JGR Solid Earth

RESEARCH ARTICLE
10.1029/2019JB019184

Key Points:
- First insights into the crustal structure of the northeastern Lau Basin, along a 290 km transect at 17° 20′S
- Crust in southern Fonualei Rift and Spreading Center was created by extension of arc crust and variable amount of magmatism
- Magmatic underplating is present in some parts of the southern Niuafo'ou Microplate

Supporting Information:
- Supporting Information S1

Correspondence to:
F. Schmid,
fschmid@geomar.de

Citation:
Schmid, F., Kopp, H., Schnabel, M., Dannowski, A., Heyde, I., Riedel, M., et al. (2020). Crustal structure of the Niuafo'ou Microplate and Fonualei Rift and Spreading Center in the northeastern Lau Basin, Southwestern Pacific. *Journal of Geophysical Research: Solid Earth*, *125*, e2019JB019184. https://doi.org/10.1029/2019JB019184

Received 3 DEC 2019
Accepted 26 MAY 2020
Accepted article online 29 MAY 2020

Crustal Structure of the Niuafo'ou Microplate and Fonualei Rift and Spreading Center in the Northeastern Lau Basin, Southwestern Pacific

F. Schmid[1], H. Kopp[1,2], M. Schnabel[3], A. Dannowski[1], I. Heyde[3], M. Riedel[1], M. D. Hannington[1,4], M. Engels[3], A. Beniest[5], I. Klaucke[1], N. Augustin[1], P. A. Brandl[1], and C. Devey[1]

[1]GEOMAR, Helmholtz Centre for Ocean Research, Kiel, Germany, [2]Department of Geosciences, Kiel University, Kiel, Germany, [3]BGR, Federal Institute for Geosciences and Natural Resources, Hanover, Germany, [4]Department of Earth Sciences, University of Ottawa, Ottawa, ON, Canada, [5]Department of Earth Sciences, Vrije Universiteit Amsterdam, Amsterdam, The Netherlands

Abstract The northeastern Lau Basin is one of the fastest opening and magmatically most active back-arc regions on Earth. Although the current pattern of plate boundaries and motions in this complex mosaic of microplates is reasonably understood, the internal structure and evolution of the back-arc crust are not. We present new geophysical data from a 290 km long east-west oriented transect crossing the Niuafo'ou Microplate (back-arc), the Fonualei Rift and Spreading Center (FRSC) and the Tofua Volcanic Arc at 17°20′S. Our *P* wave tomography model and density modeling suggest that past crustal accretion inside the southern FRSC was accommodated by a combination of arc crustal extension and magmatic activity. The absence of magnetic reversals inside the FRSC supports this and suggests that focused seafloor spreading has until now not contributed to crustal accretion. The back-arc crust constituting the southern Niuafo'ou Microplate reveals a heterogeneous structure comprising several crustal blocks. Some regions of the back-arc show a crustal structure similar to typical oceanic crust, suggesting they originate from seafloor spreading. Other crustal blocks resemble a structure that is similar to volcanic arc crust or a "hydrous" type of oceanic crust that has been created at a spreading center influenced by slab-derived water at distances <50 km to the arc. Throughout the back-arc region, we observe a high-velocity (Vp 7.2–7.5 km s^{-1}) lower crust, which is an indication for magmatic underplating, which is likely sustained by elevated upper mantle temperatures in this region.

1. Introduction

The Lau Basin in the southwestern Pacific is one of the most volcanically active submarine regions on Earth (e.g., Chadwick et al., 2019; German et al., 2006). It is also the site where processes of back-arc basin formation were first proposed by Karig (1970). The basin is located west of the Tonga subduction zone, between the active Tofua Volcanic Arc in the East and the remnant arc of the Lau Ridge in the West (Figure 1). The opening of the basin started ~6 Ma ago, initiated by a still on-going roll back of the Tonga subduction zone (Hawkins, 1995). The Lau Basin has a characteristic triangular shape with the greatest width in the north, narrowing to the south. From south to north, the overall opening rates increase and so does the tectonic complexity (Bevis et al., 1995; Taylor et al., 1996). Chase (1971) was the first to postulate the presence of several tectonic plates and triple junctions in the northern Lau Basin. The investigation of bathymetry and inversion of magnetic data from the southern Lau Basin suggests that crust accreted along discrete spreading centers, which have functioned similarly to midocean ridges since at least 4 Ma (Taylor et al., 1996). However, whereas the magnetic pattern is relatively clear south of 18°S, it is more complex to the North where the lack of high-quality magnetic data prevents a straightforward magnetic anomaly inversion (Sleeper & Martinez, 2016). The southern Lau Basin and Havre Trough, which is the southward continuation of the Lau Basin, have been targeted by a number of geophysical experiments, (e.g., Arai & Dunn, 2014; Bassett et al., 2016; Crawford et al., 2003; Dunn et al., 2013; Dunn & Martinez, 2011; Tontini et al., 2019). In contrast, little is known

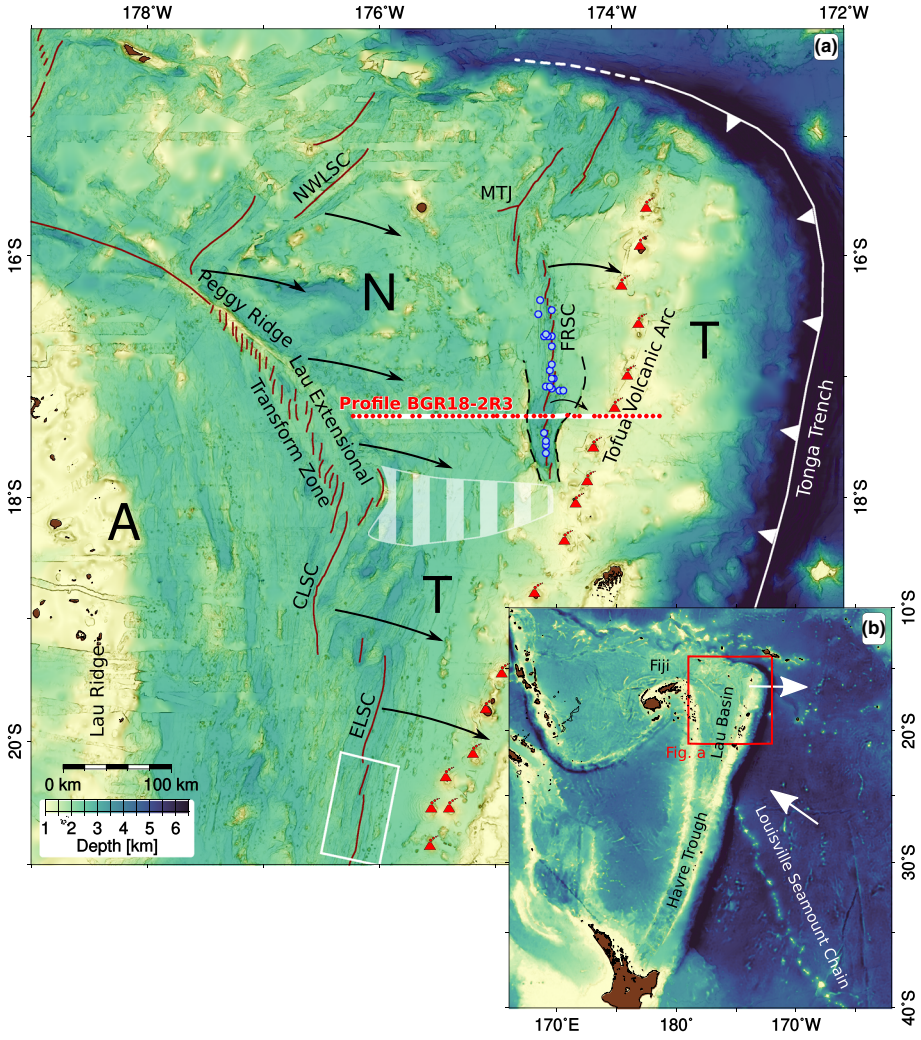

Figure 1. Bathymetry of the northern Lau Basin with tectonic plates and plate boundaries indicated. Map (a) shows the Niuafou'ou Microplate (N) with surroundings. A = Australian Plate, CLSC = Central Lau Spreading Center, ELSC = Eastern Lau Spreading Center, FRSC = Fonualei Rift and Spreading Center, MTJ = Mangatolu Triple Junction, NWLSC = Northwestern Lau Spreading Center, T = Tonga Plate. Our survey line (BGR18-2R3) is plotted as white line with red dots indicating ocean bottom seismometer (OBS) locations. The black arrows indicate relative sense of plate motions in reference to the Australian Plate, adopted from the plate kinematic model of Sleeper and Martinez (2016). Arrows are not to scale. The hatched area highlights the aseismic diffuse southern boundary of the Niuafo'ou Microplate (Baxter et al., 2020), and the white rectangle indicates the Eastern Lau Spreading Center (ELSC) region investigated by Dunn and Martinez (2011) and Arai and Dunn (2014). Blue circles show dredge locations from Keller et al. (2008) yielding basalts and basaltic andesites. The dredged lavas are geochemically indistinguishable from the lavas of the proximal volcanic arc (Keller et al., 2008). The bathymetry data in both maps is compiled from the Global Multi-Resolution Topography Synthesis of (Ryan et al., 2009) and expedition SO267 data (Hannington et al., 2019). A map showing the extent of SO267 data is provided in Figure S1. Red square in overview map (b) gives the location of map (a). White arrows indicate relative plate motions of the Pacific and Tonga plates at the Tonga Trench.

about the crustal structure of the northeastern Lau Basin including the Niuafo'ou Microplate and the Fonualei Rift and Spreading Center (FRSC; Figure 1). Unique to the Lau Basin is the synchronous coexistence of two parallel zones of extension—the Lau Extension Transform Zone (Baxter et al., 2020) and the FRSC (Sleeper et al., 2016; Sleeper & Martinez, 2016)—that both accommodate E-W extension (Figure 1). Such a configuration of two parallel zones of extension does not exist in any other back-arc system. In the northeastern Lau Basin, the tectonic structure and plate kinematics are highly complex and several aspects therein remain unresolved (Sleeper & Martinez, 2016; Zellmer & Taylor, 2001).

Important open questions include the following:

1. How thick is the back-arc crust of the Niuafo'ou Microplate, in comparison to typical oceanic crust and compared to crust in other intraoceanic back-arc regions?
2. How does the Vp-depth distribution, indicative for lithology of different crustal layers, compare to other back-arc regions?
3. Where, when, and how was the back-arc crust in the northeastern Lau Basin created?

To address the above questions, we acquired new refraction and multichannel reflection seismic, magnetic, gravimetric, multibeam bathymetry, and sediment echosounder data on a 290 km long profile crossing the Niuafo'ou Microplate, the FRSC, and the Tofua Volcanic Arc at 17°20′S (profile BGR18-2R3, Figure 1). All data were acquired during RV Sonne expedition SO267 (ARCHIMEDES I; Hannington et al., 2019) from December 2018 to January 2019. The results allow a first quantification of the crustal thickness of the Niuafo'ou Microplate and the processes of back-arc formation, within the larger regional geodynamic context of the northeastern Lau Basin.

2. Tectonic Setting of the Northeastern Lau Basin

2.1. Plate Kinematic Models

A first kinematic model of the current plate configuration and plate motions in the Northern Lau Basin was established by Zellmer and Taylor (2001) on the basis of geodetic measurements, seismicity, backscatter imagery, and ship-based bathymetry. This model proposes a three-plate configuration with the Niuafo'ou Microplate (N) in the center separated by the Peggy Ridge—Lau Extensional Transform Zone (LETZ) from the Australian Plate in the West and the Mangatolu Triple Junction—FRSC boundary from the Tonga Plate (T) in the East (Figure 1). The southern boundary of the Niuafo'ou Microplate is diffuse, and a local seismicity study did not show distinct seismic activity between the FRSC and the LETZ (Baxter et al., 2020; Conder & Wiens, 2011). The Northwestern Lau Spreading Center (NWLSC) marks the western portion of the northern boundary of the Niuafo'ou Microplate, but farther East, the plate boundary is not well defined (Figure 1). The initial plate kinematic model of Zellmer and Taylor (2001) predicted deformation rates >40 mm year^{-1} at the diffuse southern boundary, which disagrees with the scarce seismicity in this area (Sleeper & Martinez, 2016). This apparent contradiction of having no seismicity at an active plate boundary motivated Sleeper and Martinez (2016) to reanalyze the early plate kinematic model of Zellmer and Taylor (2001). The updated kinematic model predicts much slower (~ 8 mm year^{-1}) opening rates at the southern tip of the FRSC (~17°54′S) which is in better agreement with the lack of local seismicity in the area between the southern FRSC and LETZ (Sleeper & Martinez, 2016). The Euler pole for the boundary between plates N and T (FRSC) of the Zellmer and Taylor (2001) locates at 20°S and migrates north to 18.5°S in the more recent model of Sleeper and Martinez (2016). The FRSC constitutes the plate boundary between the Niuafo'ou and Tonga plates. The current tectonic setting of the FRSC is characterized by pure extension (Baxter et al., 2020; Zellmer & Taylor, 2001).

2.2. Fonualei Rift and Spreading Center

The FRSC is a southward propagating divergent plate boundary at which the opening rates decrease from north to south (Sleeper & Martinez, 2016; Zellmer & Taylor, 2001). In the south, the spreading axis approaches the volcanic front, with a minimum separation of just 25 km near the southern tip of the FRSC (Figure 1). At the southern end of the FRSC high standing, rifted margins are visible (dashed lines in Figure 1a). However, the nature of tectonic and magmatic processes at the FRSC and their similarity with typical back-arc spreading centers remains unclear. Sleeper and Martinez (2016) emphasize that the axial morphology abruptly alters at about 17°S from a continuous volcanic ridge north of this boundary to isolated volcanic cones surrounded by anomalously deep seafloor to the south of 17°S. At 17°S, the FRSC axis is located at approximately 50 km distance to the volcanic arc (Figure 1). These abrupt morphological changes may reflect along-axis flux and focusing of melt beneath the volcanic cones, as the opening rates decrease and the FRSC axis approaches the volcanic arc (Brandl et al., 2020; Sleeper et al., 2016).

Dredged lavas from the FRSC show geochemical signatures that are almost identical to lavas from the near arc volcanoes (Escrig et al., 2012; Keller et al., 2008). Several hydrothermal sites have been identified along the FRSC (some of which are confirmed and some are only inferred) suggesting that the occurrence of hydrothermal sites

per 100 km spreading axis is unusually high compared to midocean ridges but comparable to other arc-influenced back-arc spreading centers (Baker et al., 2019; German et al., 2006; Kim et al., 2009).

2.3. Crustal Structure at the ELSC

The ELSC represents the southern continuation of the Central Lau Spreading Center (CLSC) and is, like the FRSC, a southwards propagating back-arc spreading center at a decreasing distance to the volcanic arc front, from north to south (Figure 1). The ELSC region at 20°-21°S has been investigated by a large-scale 3-D seismic experiment (L-SCAN survey; location is indicated by the white rectangle in Figure 1) which resulted in a very detailed analysis of the crustal structure and crustal accretion processes in this region (Arai & Dunn, 2014; Dunn & Martinez, 2011; Eason & Dunn, 2015). Back-arc crust created at less than 50 km from the volcanic arc front is unusually thick (8 and 9 km) and includes a thick upper crustal layer of low *P* wave velocities (3.4–4.5 km s^{-1}) and a lower crustal layer of abnormally high-velocity (7.2–7.5 km s^{-1}; Arai & Dunn, 2014; Dunn & Martinez, 2011). Such crust is labeled as Domain II crust and also regarded as "hydrous" crust by Arai and Dunn (2014). What caused the unusual composition and Vp-depth distribution of this crust is the input of slab-derived water into the subaxial melting regime of the back-arc spreading center (Arai & Dunn, 2014; Dunn & Martinez, 2011). The numerical models of mantle melting presented in Eason and Dunn (2015) suggest that slab-derived water does not only enhance mantle melting but also affects magmatic differentiation and crustal accretion processes. The water in the mantle source region is also entrained into the melt ascending to crustal depths and leads to the formation of basalts with elevated porosity. Such basalts of increased porosities have decreased *P* wave velocities (Hirth & Kohlstedt, 1996). Numerical modeling results indicate that ~0.5–1.0 wt% of water in parental mantle melts may lead to crystallization of mafic cumulates in the lowermost crust, which is characterized by a layer of unusually high velocities (7.2–7.5 km s^{-1}) in the lower crust (Arai & Dunn, 2014; Eason & Dunn, 2015). The seismic results from the ELSC further indicate that back-arc crust created at distances greater than 70 km from the volcanic arc front is significantly thinner (~7 km) and does not reveal the thick low-velocity layer in the upper crust nor a high-velocity layer in the lower crust (Arai & Dunn, 2014; Dunn & Martinez, 2011). Such crust is labeled as Domain III and shows a thickness and Vp-depth distribution that is more similar to typical oceanic crust than crust in Domain II.

Here, we make use of the 3-D seismic survey results from the ELSC and directly compare the Vp-depth distributions along profile BGR18-2R3 to those of Domain II and Domain III crust at the ELSC to compare the seismic crustal structure in both back-arc regions and to estimate the impact of slab-derived water during crustal production in our survey area.

3. Data

The following text sections provide a concise overview of the geophysical methods applied in data acquisition, processing, and seismic tomography. Additional details about the data acquisition are available in the SO267 cruise report (Hannington et al., 2019).

3.1. Bathymetric Data

Bathymetric data were acquired during RV Sonne expedition SO267 using a hull-mounted Simrad EM122 system in a 0.5° by 1° configuration and a 130° total opening angle. Raw data have been filtered using a triangulation method and subsequently edited manually. Slow survey speeds of less than five knots together with equidistant and dual-ping mode allowed calculating a bathymetric grid with 50 m grid cell size.

3.2. Refraction Seismic Data

We deployed 47 OBSs of the GEOMAR instrument pool at an average spacing of 6 km along profile BGR18-2R3 (Figure 1). Each OBS included a 4.5 Hz three-component geophone and a High Tech Inc ULF/PCA hydrophone. Seismic data were recorded at a sampling rate of 250 Hz. The seismic source consisted of 12 G-guns with a total volume of 84 l that were combined in two clusters and synchronously fired every 150 m along the profile. A GPS receiver mounted on the airgun flotation allowed the positioning of the seismic source for each shot. The seafloor location of the OBS was determined by fitting the direct wave arrivals. Processing of OBS data included cutting the continuous stream into single shot traces, a predictive deconvolution of the source signal and time- and offset dependent Butterworth filtering of traces. The filter pass-bands were optimized to enhance lower frequencies at increasing offsets travel times. The filter for near

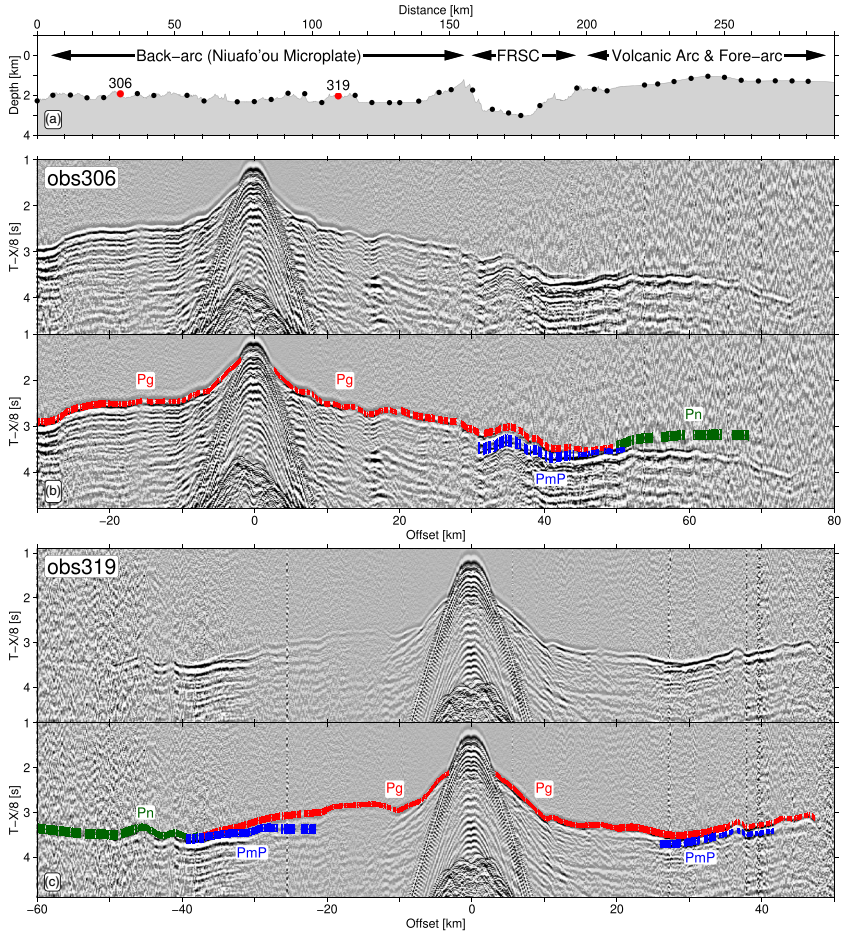

Figure 2. (a) Seafloor topography along profile BGR18-2R3 with black dots showing OBS locations. Panels b and c show refraction seismic shot gathers for stations 306 (panel b) and 319 (panel c) sitting on back-arc crust. Colored bars show phase arrival picks (vertical extent gives uncertainty).

offsets with short phase travel times had a pass-band at 8–30 Hz and the filter for far offsets and large phase travel times had a pass-band at 3–15 Hz. Forty-three of the deployed OBS returned useable data of good quality, with the best signal-to-noise ratio present at stations sitting on back-arc crust and on the volcanic arc, yielding clear phase arrivals to maximum offsets of 60 km (Figures 2 and 3). We manually picked the phase arrivals and determined picking errors, which also include possible phase shifts caused by filtering and predictive deconvolution (Table 1). Generally, the pick uncertainties increase with offset, which is attributed to decreasing signal-to-noise ratios at larger offsets.

3.3. MCS Reflection Data

To acquire the multichannel seismic (MCS) line presented in Figure 4f, we sailed the profile line a second time with a decreased shot interval of 50 m. The seismic sources were operated in the same configuration as for the refraction seismic operations. We used a seismic streamer with an active length of 3,900 m and a hydrophone-group interval of 12.5 m resulting in 312 channels. To minimize the effects of the source array, we applied a deconvolution to the raw data. This process uses the source signature, which was recorded for each shot on an auxiliary channel, to design a shot-dependent deconvolution filter. This process successfully supressed the bubble pulse and converted the recorded signal to minimum phase. Additional seismic processing included the following steps: Binning to common depth points (CDP interval of 6.25 m), band-pass filtering (main frequencies 6 to 60 Hz), multiple suppressions (using surface related multiple suppression), true amplitude recovery (to correct for spherical divergence), moveout-correction of CDP-gathers, stacking and poststack Kirchhoff time migration. To facilitate the interpretation of crustal structures, we finally produced

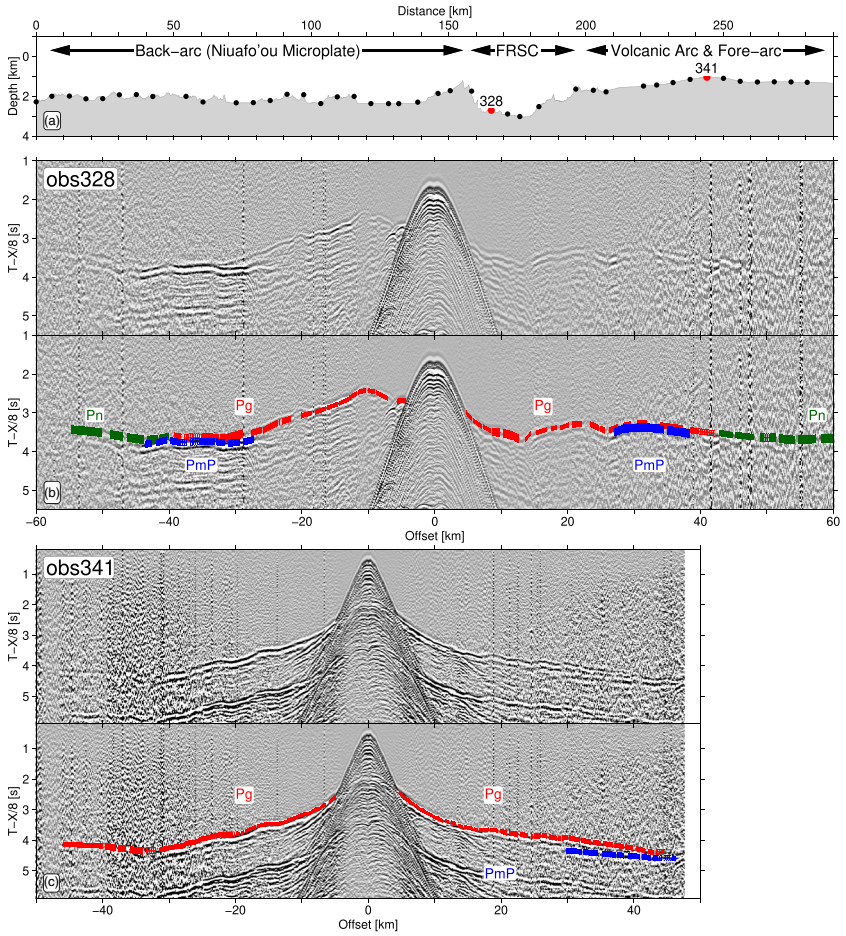

Figure 3. (a) Seafloor topography along profile BGR18-2R3 with black dots showing OBS locations. Panels b and c show refraction seismic shot gathers for stations 328 (panel b) within the FRSC and station 341 (panel c) sitting on volcanic-arc crust. Colored bars show phase arrival picks (vertical extent gives uncertainty).

a depth-converted section. The ensemble average refraction seismic *P* wave tomography model (Figure 4a) was used for the final depth-conversion processing step.

3.4. Gravity Data

We acquired gravity data continuously throughout the entire SO267 expedition with a sea gravimeter system KSS32-M (serial No. 22). The observed gravity data were tied to the International Gravity Standardization Net IGSN 71 by connection measurements conducted in the port of Suva (Fiji), prior and after the cruise. After the termination of the cruise, the instrumental drift was determined to +4.7 mGal in 46 days (Hannington et al., 2019). This drift rate is relatively high but the mismatch of measurements from repeated passes along the profile BGR18-2R3 is smaller than 1.0 mGal (Figure S4 in the supporting information). The observed drift is within the range of drift rates estimates for this instrument on previous cruises, and the gravity data were corrected for the observed drift, accordingly. We subtracted the normal gravity (GRS80) and the Eötvös effect in order to obtain free-air gravity anomalies. Exhaustive details about the gravity data processing and data quality are provided in the SO267 cruise report (Hannington et al., 2019) and Text S2. In Figure 6a, we plot our gravity data against satellite data, extracted from the global grid of Sandwell et al. (2014).

Table 1
Number of Picks per Phase, Picking Uncertainty, RMS Misfit and Chi^2 Values of Different Phase Arrivals Associated With the Ensemble Average Tomography Model, Presented in Figure 4a

Phase	No. of picks	Pick uncertainty [ms]	RMS [ms]	Chi^2
Pg	18,234	40–70	69	1.13
PmP	5,355	70	62	0.79
Pn	3,305	80	85	1.02

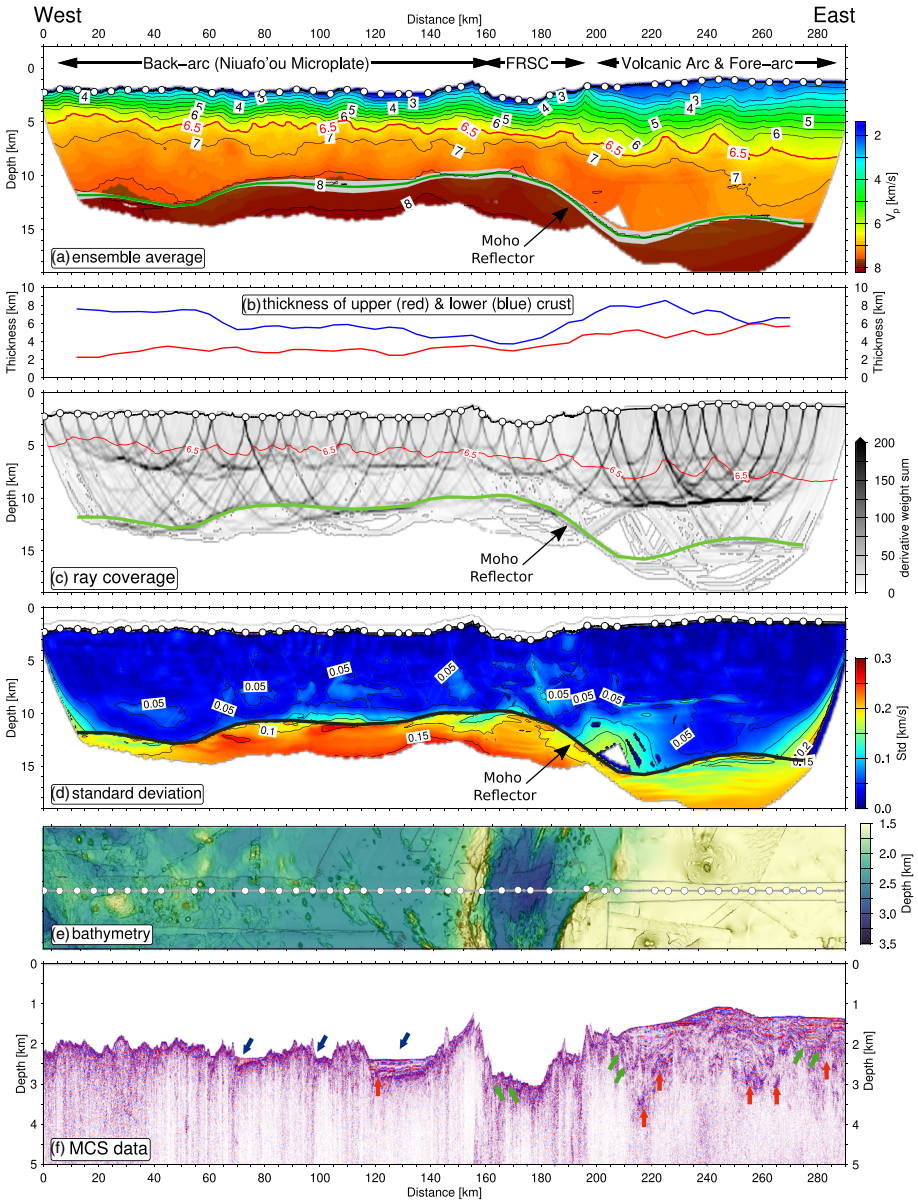

Figure 4. (a) Final *P* wave tomography model (ensemble average of 100 Monte-Carlo runs) for profile BGR18-2R3 with major tectonic regions indicated on top. Contour interval is 0.5 km s^{-1}. We define the 6.5 km s^{-1} contour as the boundary between the upper and lower crust (marked by the red line). The gray zone around the Moho reflector indicates the depth uncertainty estimated from the sum of Monte-Carlo runs. (b) Thickness of the upper crust ($2.5 < Vp < 6.5$ km s^{-1}) and lower crust (range between 6.5 km s^{-1} contour and modeled Moho reflector). (c) Derivative weight sum for individual nodes of the model grid, representing the ray coverage. The red line represents the 6.5 km s^{-1} contour, which marks the boundary between upper and lower crust. Solid green line represents the Moho reflector. A plot with ray paths for selected stations is provided in Figure S2. (d) Uncertainty of the final tomography model, given by the standard deviation of Monte-Carlos runs. Contours are plotted at 0.05 km s^{-1} interval. Solid black line represents the Moho reflector. Note, higher uncertainty in the upper mantle is related to the reduced ray coverage here. (e) Bathymetry along the profile (gray line) with white dots showing ocean bottom seismometer locations. (f) Multichannel seismic reflection data acquired along the same profile line. Depth-conversion was performed based on the final tomography model, panel a. Blue arrows indicate the location of sedimentary basins on back-arc crust. Red arrows indicate the location of flat-lying reflectors of high-amplitude, likely representing magmatic sills. Green arrows indicate the location of normal faults, eastwards dipping in the western part of the FRSC and westwards dipping within the volcanic-arc.

Generally, the mismatch of our ship-based data and the satellite data was smaller than 5 mGal.

3.5. Magnetic Data

Marine magnetic data presented here were acquired during expedition SO267 with a towed marine magnetics SeaSpyII gradiometer system. Exhaustive technical detail about the system specifications and the data acquisition may be found in the SO267 cruise report (Hannington et al., 2019). The magnetic anomaly data acquired along profile BGR18-2R3 do not include any significant planetary noise, due to the low planetary magnetic activity at the time of surveying.

4. Modeling and Refraction Seismic Results

4.1. Refraction Seismic Tomography

An initial 2-D *P* wave velocity model was achieved by iterative forward modeling of phase arrivals with the RAYINVR software (Zelt & Smith, 1992). The initial velocity model included shipborne bathymetry data and the thickness of sediment layers from the MCS data, acquired on a coincident profile line (see section 3.3). In this step, the acoustic basement reflector was picked in the time migrated MCS image, wherever discernible and interpolated in between. The travel times of the basement reflector were then converted to depth assuming an average velocity of 1.8 km s^{-2} in the sediment layer. The initial velocity model is presented in Figure S3. The initial velocity model had an average RMS travel time misfit of 0.13 s and a normalized χ^2 value of 4.2.

The initial *P* wave velocity model served as a starting model for the tomographic inversion of refracted and reflected phases with the TOMO2D software of Korenaga et al. (2000). The TOMO2D software performs ray-tracing and calculates travel times via a combination of the graph and ray-bending methods (Korenaga et al., 2000). The computational grid for the tomography is parameterized in the form of a sheared mesh hanging below the seafloor that has a horizontal node spacing of 300 m and a variable vertical node spacing of 100 m near the seafloor, linearly increasing to 340 m at 29 km depth.

To accomplish the *P* wave tomography, we followed a two-step approach. In the first step, only crustal refractions (Pg) and Moho reflections (PmP) were inverted in a separate tomographic model. In a second step, mantle refractions (Pn) were added to the input data, and the crustal velocities and thickness were kept constant (overdampened) to achieve the second model, which includes upper mantle velocities. An initial inversion including all phases, (Pg, PmP, Pn) did not include a clear step in Vp at the Moho interface and showed a poor performance, in terms of RMS misfit. This issue was overcome by using the step-wise tomographic inversion. The smoothing of the tomographic inversion with the TOMO2D software is steered through a so-called correlation length file, which is provided and explained in the Supporting Information. We employed a Monte-Carlo approach by using 100 different starting models (created by randomly perturbing the initial velocity model within conceivable ranges) and then calculating ensemble averages for the 100 output models. In this step, only models were accepted with a χ^2 values below a threshold of 1.5. Typically, three inversion iterations were necessary until the χ^2 value dropped below this threshold. Ray coverage and model uncertainties are shown in Figures 4c and 4d. Model uncertainties, given by the standard deviation of all output models, are generally smaller than 0.1 km s^{-1} for most of the crust and around 0.2 km s^{-1} for the upper mantle, where ray coverage is less dense. The number phase picks, the average RMS misfit, and χ^2 values of different phases in the ensemble average model are presented in Table 1.

4.2. Checkerboard Resolution Tests

We implemented a series of three checkerboard tests to constrain the ability of the tomography model to recover the amplitude and location of velocity anomalies in the crust. We started the inversion with the unperturbed ensemble average tomography model (Figure 4a) and the identical smoothing parameters as used for the real data inversion. This study focuses on the crustal structure motivating our use of Pg and PmP phases in the checkerboard tests. Pn phases that touch the upper mantle were not included in the checkerboard tests. The scarcity of Pn phases did not admit a robust investigation of the upper mantle structure in the real data model and checkerboard tests. A minimum in RMS travel time residuals of 0.015 s (Pg + PmP phases) was achieved with the checkerboard models after three iterations. The checkerboard testing results indicate that 10 × 2 km sized anomalies of 5% perturbation are well resolved from the seafloor downwards to about 6 km below the sea surface. Anomalies sized 15 × 3 km with 5% perturbation are

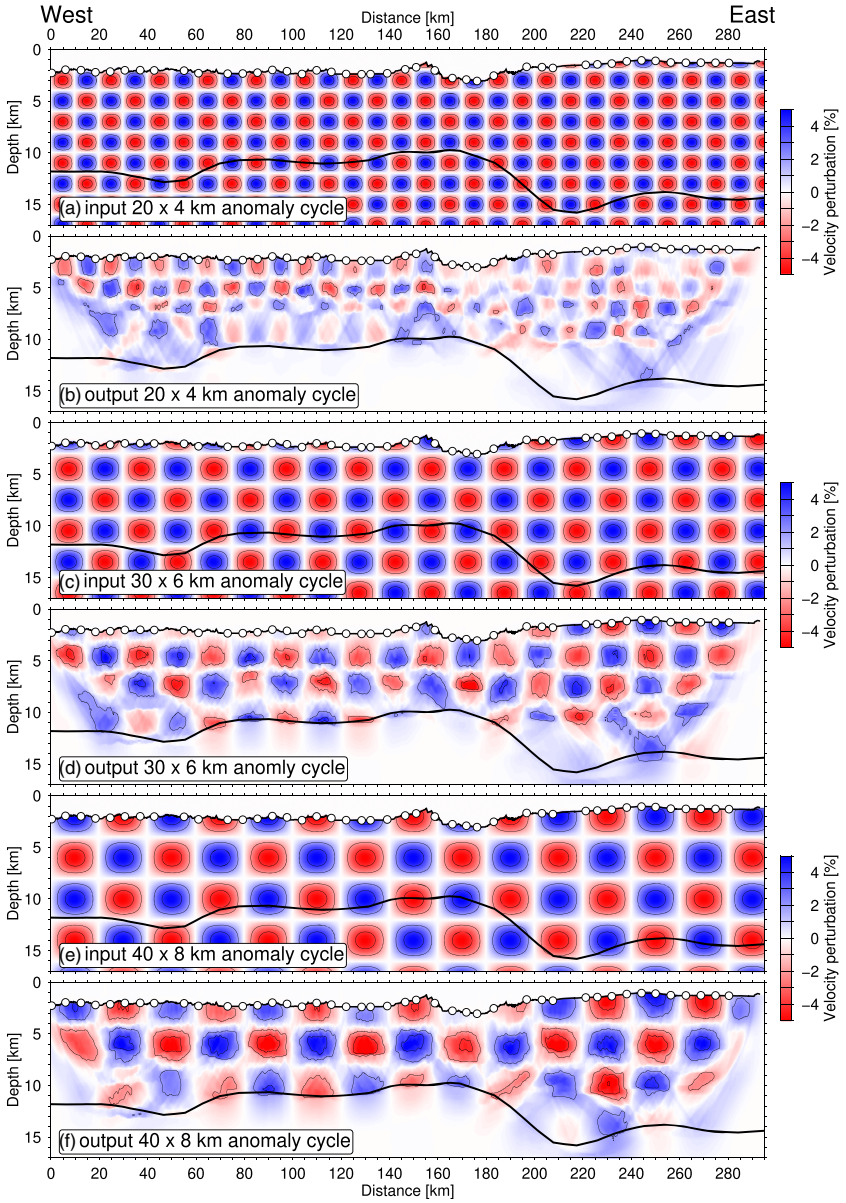

Figure 5. Three checkerboard tests performed with different sizes of synthetic anomalies. The solid black lines represents the Moho reflector. (a) and (b) show the input and output models for a test with anomalies cycling at 20 × 4 km wavelength in horizontal and vertical dimensions, respectively. (c) and (d) present a test with anomalies cycling at 30 km in horizontal and 6 km in vertical domain. (e) and (f) present a test with anomalies cycling at 40 km horizontally and 8 km vertically.

well resolved down to about 9 km below sea surface and 20 × 4 km sized anomalies of 5% perturbation are well resolved to about 12 km below the sea surface (Figure 5). While the shape and size of anomalies is well restored in the uppermost kilometers of the crust, the output model becomes blurred at the lower crustal depths, in particular near the ends of the profile (Figure 5). There is some slight smearing of anomalies from above the Moho reflector to the region immediately below the Moho, which is an effect of the model smoothing.

4.3. Refraction Seismic Results

The offset range at which high amplitude Moho reflections (PmP phases) appear in shot gathers (Figures 2 and 3) already provides a rough estimate of the crustal thickness. The observation of high-amplitude reflections from the Moho interface indicates that a strong impedance contrast is present at the crust-mantle

boundary along most of the profile. On the back-arc, PmP phases occur at offsets between 25 and 50 km (Figure 2) and on the volcanic arc PmP phases appear at offsets between 30 and 60 km (Figure 3), indicating a thickened arc crust.

The ensemble average *P* wave tomography model, together with the thickness of crustal units, ray coverage, velocity uncertainties, and the results of the checkerboard resolution tests are presented in Figures 4 and 5. The ray coverage is densest in the upper crust and the upper part of the lower crust, yielding the smallest velocity uncertainties (<0.1 km s^{-1}) and stable results of the checkerboard tests at these depths. In the volcanic arc, the upper crust is covered by ample ray crossings, but the lower crust is less well sampled, resulting in higher uncertainties and a slightly poorer performance of the checkerboard test. The number of rays penetrating the uppermost mantle is considerably lower than in the crust, causing an increase in velocity uncertainties with around values of 0.2 km s^{-1}.

We define the upper crust (seismic Layer 2) as the region between the 2.5 s^{-1} isovelocity contour (that correlates with the top of the igneous basement) and the depth of the 6.5 km s^{-1} isovelocity contour (red line in Figure 4a). The 6.5 km s^{-1} contour corresponds to the lower depth limit of the steep upper-crustal velocity gradient, and is commonly considered as the boundary between oceanic Layers 2 and 3 (Christeson et al., 2019). We define the lower crust as the area between the 6.5 km s^{-1} isovelocity contour and the Moho reflector. It should be noted that this definition of upper and lower crust does not necessarily represent a distinct petrological boundary and is mainly introduced to illustrate structural changes along the profile and provide a framework for the later density modeling.

The upper crust (Layer 2) is thinnest (2.2 km) near the western end of profile BGR18-2R3 and has an average thickness of 3.0 km across the back-arc region (Figure 4b). Eastwards of the FRSC, the upper crust constantly increases in thickness, reaching a maximum of 5.9 km near the eastern end of profile BGR18-2R3. In contrast, the lower crust is unusually thick (~7.5 km) near the western end of profile BGR18-2R3 with an average thickness of 5.0 km between 70 and 150 km distance along the profile (Figure 4b).

4.4. Forward Modeling of Gravity/Density

We established an initial density model for the crust and upper mantle along profile BGR18-2R3 by taking the geometry of the upper and lower crustal units from the ensemble average velocity model (Figure 4a). The initial density model is composed of five layers, and each layer was assigned a constant density (Figure 6c). The uppermost layer includes the water column with a density of 1.03 Mg m^{-3}. The second layer comprises sedimentary units along the profile with the lower boundary provided by the 2.5 km s^{-1} contour of the tomography model. Since detailed knowledge about the density of sediments in the survey area is absent we adopt the Vp-density relations of Brocher (2005) for sedimentary rocks that suggest a density of 2.05 Mg m^{-3} for the average Vp of 1.9 km s^{-1} observed in the sedimentary units. The third layer represents the upper crust, and its boundaries are given by the 2.5 and 6.5 km s^{-1} velocity contours. Presuming a dominance of basaltic rocks in this layer we incorporate a density of 2.70 Mg m^{-3} in agreement with the Nafe-Drake curve published in Brocher (2005), originating from (Ludwig et al., 1970). This value of 2.70 Mg m^{-3} is in agreement with the published values of Carlson and Raskin (1984). The fourth layer, representing the lower crust, is located between the 6.5 km s^{-1} contour and the Moho reflector. Carlson (2004) shows that densities of gabbroic rocks in the lower oceanic crust range between 2.82 and 3.00 Mg m^{-3}, which motivated our choice of a 2.90 Mg m^{-3} density. The fifth and lowermost layer represents the upper mantle. The upper boundary of this layer is given by the Moho reflector and the lower boundary is given by the model boundary at 40 km depth below sea surface. Typical upper mantle densities range between 3.25 and 3.35 Mg m^{-3} (Kern, 1993) motivating our choice of a constant density of 3.30 Mg m^{-3} in this layer. The 2-D density model is realized on a regular grid with a grid point spacing of 0.25 km in the horizontal and 0.1 km in the vertical domain. We calculated the theoretical gravity anomalies along the profile with the routine described in Korenaga et al. (2001).

The computed gravity signature of the initial density model (of constant layer densities) had an average RMS misfit of 22.7 mGal compared to the vessel based free air anomaly (FAA) data (Figure 6b). The misfit is small (<3.0 mGal) in the western half of the profile but from 140 km onwards to the eastern end the misfit constantly increases (Figure 6b). This large misfit is caused by a long-wavelength positive anomaly of ~80 mGal amplitude, which is centered above the broad fore-arc region and was only partly covered by

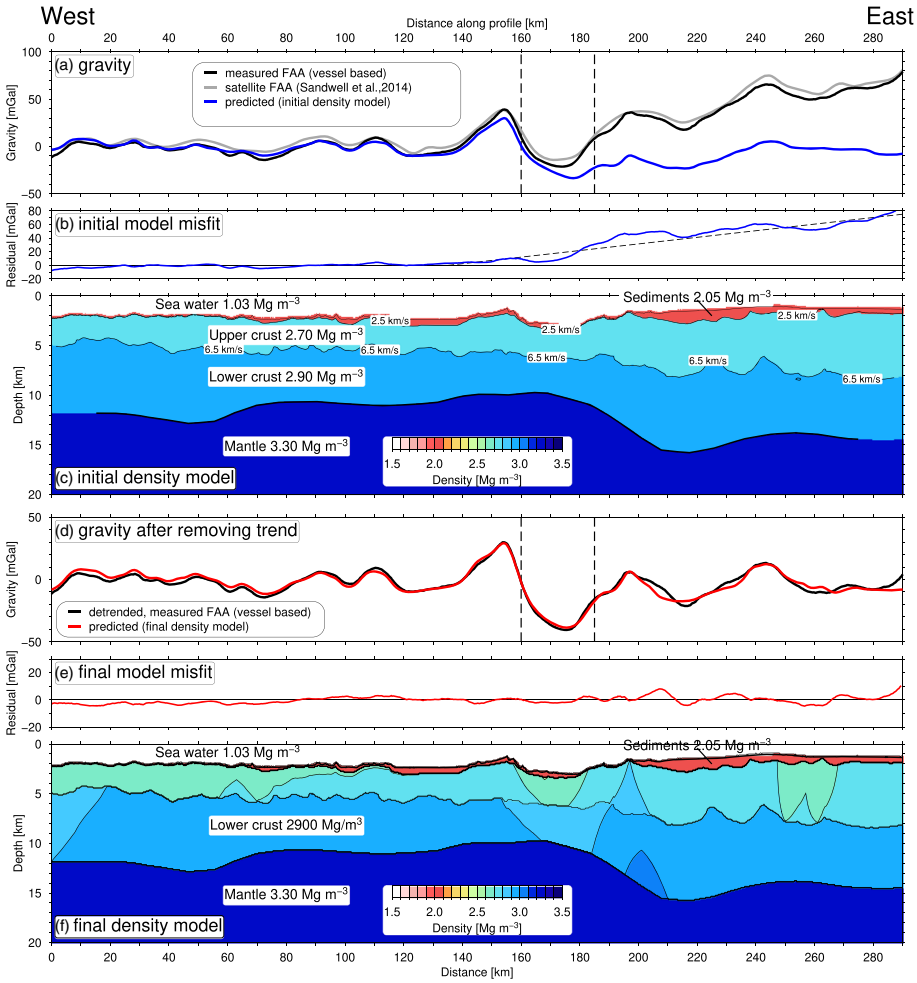

Figure 6. (a) Vessel based gravity free air anomaly (FAA; black line), satellite-based FAA from Sandwell et al. (2014; gray line) and modeled gravity anomalies from the initial density model (blue line) along profile BGR18-2R3. Vertical dashed lines in panels a and d indicate the extent of the FRSC rift valley. (b) Misfit of observed (vessel based) FAA and the gravity anomalies predicted by the initial density model (blue line). The dashed line indicates the linear trend which has been removed from the observed gravity. RMS misfit is 22 mGal. (c) Initial density model, which was constructed from velocity contours (black lines) of the final Vp tomography model. (d) Vessel-based FAA anomalies after removing the linear trend plotted in panel b and predicted density anomalies from the final density model, panel f. (e) Misfit of observed gravity anomalies predicted anomalies of the final density model, panel f. RMS misfit is 2 mGal. (f) Final density model incorporating lateral density variations in the upper and lower crust to fit the predicted gravity signals with the observed gravity signals, panel c. Contours represent density at 0.1 mg m^{-3} spacing.

our profile (Figure 6b). Given its wavelength of more than 100 km, we anticipate that this anomaly is related to structures at upper mantle depths. Similar positive gravity anomalies are commonly observed above volcanic island-arcs behind active subduction zones (Bassett & Watts, 2015). These anomalies reflect a nonisostatic contribution in the gravity signal, caused by dynamic processes associated with the sinking slab or flow in the upper mantle (Bassett & Watts, 2015). This study focuses on the crustal structure and properties. Adding capability of solving nonisostatic processes in the mantle domains to our forward gravity model is therefore beyond the scope of this paper. To still investigate short-wavelength (<50 km) gravity anomalies related to lateral density variations in the crust, we approximated this long-wavelength anomaly with a linear trend between 135 and 290 km distance along our profile (dashed line in Figure 6b) and then subtract this linear trend from the observed FAA resulting in a detrended curve (Figure 6d). After removing this linear trend, all remaining anomalies could be fitted by including a number of lateral density changes in the upper and lower crust of the final density model (Figure 6f). The misfit of observed and predicted gravity anomalies in the final density model (Figures 6e and 6f) was reduced to an RMS value of 1.6 mGal. The most prominent lateral changes to the density structure were applied to the crust

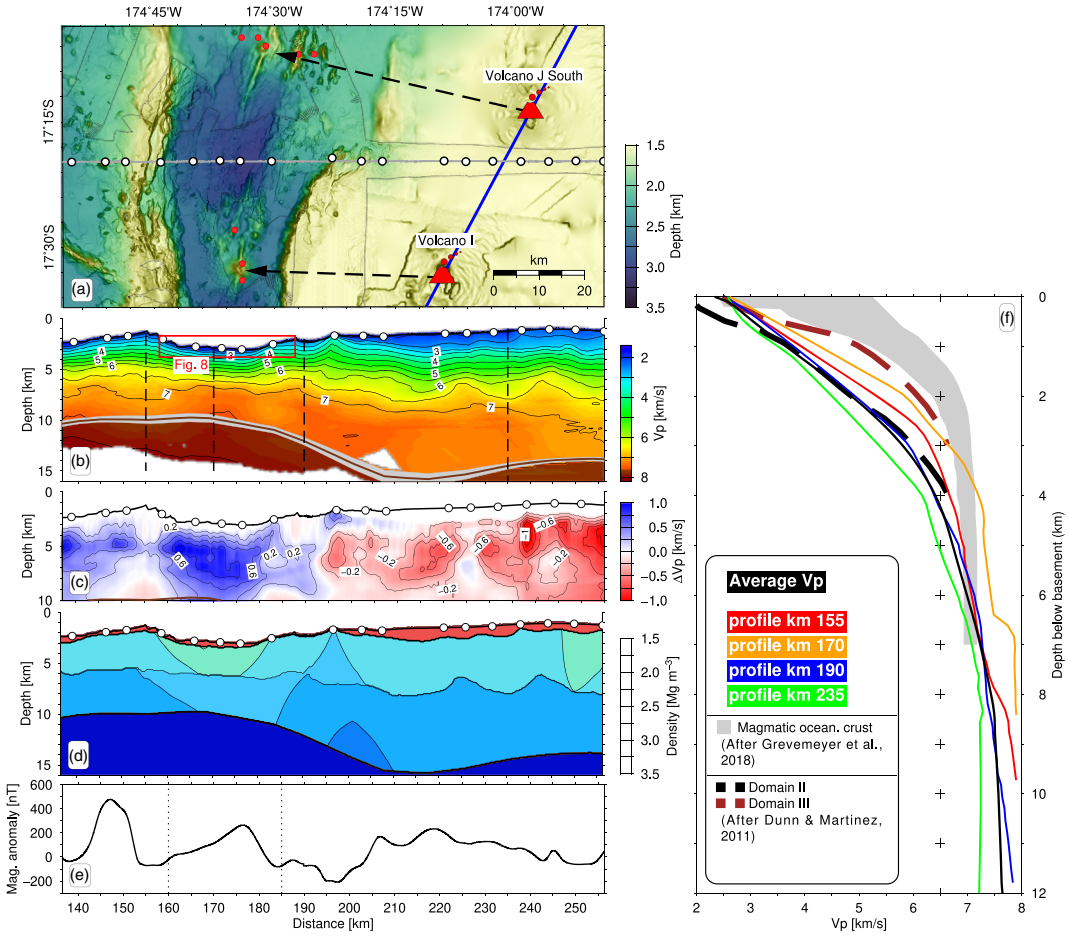

Figure 7. (a) Bathymetry of the FRSC and Tonga Arc region with profile BGR18-2R3 (gray line, white circles representing OBS locations). Red trapezoids show locations of arc volcanoes, and arrows indicate volcanic centers of the FRSC, potentially fed by a common magma reservoir (Sleeper et al., 2016). Solid blue line is the location of the arc volcanic front. Red dots show dredge locations yielding basalts and basaltic andesites (Keller et al., 2008). In terms of geochemistry the dredged lavas are indistinguishable from the lavas of the proximal volcanic arc (Keller et al., 2008). (b) Ensemble average *P* wave tomography model for the profile section traversing the above map with dashed lines indicating locations of 1-D profiles shown in panel f. (c) Velocity deviation in the igneous basement from an average 1-D Vp-depth profile (solid black line in panel f) in the region between 137 and 256 km distance. Contours are spaced at 0.2 km s^{-1}. Absolute values of calculated Vp deviations deeper than 10 km below the sea surface are not plotted, since the variation in crustal thickness along the profile impose a bias at these depths. (d) Final density model for the same region as panels b and c. (e) magnetic anomalies along the same section of profile BGR18-2R3 based on towed magnetometer data from the SO267 expedition (Hannington et al., 2019). The dashed vertical lines indicate the width of the FRSC inner rift valley. (f) 1-D velocity profiles for different locations along the profile, indicated by dashed lines in panel b. Other 1-D velocity profiles are taken from the publications listed at the lower left of the plot. Note, all 1-D velocity profiles are taken from below the basement surface.

underlying the FRSC, predicting a ~ 0.1 Mg m^{-3} density reduction in the upper and lower crusts here (Figure 6e). Further lateral density variations in the model were included in the upper crust near the models' western end and in the volcanic arc crust, indicating an ~0.1 Mg m^{-3} density reduction in the regions between 215–230 km and 255–265 km distance along the profile (Figure 6f). Increased densities were included in the volcanic arc region between 195–205 km and 235–245 km distance along our profile (Figure 6f). Including regions of increased density in the volcanic arc reflects the heterogeneous structure of the crust, where sediment basins alternate with intrusive bodies (section 5.1). We note that in particular, towards the eastern end of the profile the nonisostatic contribution to the gravity field by subduction related processes and our (likely over simplified) correction for this effect may cancel out any large-scale anomalies in the arc crust and our density/gravity modeling results for this region should be interpreted with care.

5. Results and Discussion

5.1. Crustal Structure and Accretionary Processes at the FRSC

Profile BGR18-2R3 traverses the FRSC between two morphologically elevated volcanic centers in a location where the seafloor is locally deepened (~3,000 m water depth; Figure 7a). The profile also crosses the volcanic arc between two volcanic centers, Volcano J South and Volcano I (Figure 7a; Keller et al., 2008). Along our profile, the crustal thickness shows strong variations, as it is only 7.0 ± 0.8 km thick at the FRSC and is 12.5 ± 0.6 km thick under the volcanic arc (Figure 4b). To identify lateral variations of *P* wave velocity (ΔVp) in the basement, we first establish an average Vp-depth profile for the igneous basement in the region between 137 and 256 km along our profile (solid black line in Figure 7f). This average 1-D Vp-depth profile is then subtracted from the basement part of the final velocity model, and the resulting velocity deviations are plotted in Figure 7c.

Beneath the rift shoulders velocities are 0.2–0.6 km s^{-1} slower than inside the FRSC (Figure 7c), suggesting compositional differences between the FRSC crust and the rift shoulders. Generally, basaltic rocks have *P* wave velocities in the order of 5.9 km s^{-1} and densities around 2.78 Mg m^{-3} at 200 MPa pressure (Christensen, 1996). Andesitic rocks have slightly lower *P* wave velocities ranging from 5.5–5.9 km s^{-1} at 200 MPa pressure and densities around 2.63 Mg m^{-3} (Christensen, 1996). Considering these laboratory values of Vp, the upper crust inside the FRSC is likely composed of basaltic rocks, and the rift shoulders are composed of more silicate-rich rocks like andesite. This is in line with recovered rock samples from the FRSC (dredge locations are plotted in Figures 1 and 7a) which are predominantly of basaltic lithology (Keller et al., 2008). The Vp-depth distribution inside the FRSC (orange line in Figure 7f) indicates that *P* wave velocities in the upper crust are higher compared to the neighboring rift shoulders and the volcanic arc, but still remain ~0.5 km s^{-1} slower than in typical oceanic crust as illustrated by the gray shaded compilation of Grevemeyer et al. (2018) in Figure 7f.

Our final density model (Figures 6f and 7d) suggests reduced densities inside the FRSC and ~0.1 Mg m^{-3} higher densities in the crust constructing the rift shoulders. However, this is at first glance in conflict with the above-mentioned compositional variations as basalts have a slightly higher density than andesites but can be explained by a thermal anomaly in the crust below the FRSC axial valley. Korenaga et al. (2001) estimated the temperature derivatives for density and Vp in oceanic rocks to be in the order of $-3.0 * 10^{-5}$ Mg m^{-3} K^{-1} and $-4.0 * 10^{-4}$ km s^{-1} K^{-1}. A reasonable temperature increase of ~400°K in the upper crust, as modeled for axial valley domains at active oceanic spreading centers (Sleep & Warren, 2014), would result in a density reduction of 0.012 Mg m^{-3} and a velocity reduction of 0.16 km s^{-1}. It should be noted that the influx of slab-derived melts at the southern FRSC (section 1) may lead to local temperature anomalies in the crust that are potentially even higher than the assumed 400 K. This agrees with our observations of Vp and density, suggesting that increased temperatures inside the FRSC may not explain the ~0.5 km s^{-1} reduction in Vp compared to typical oceanic crust (Figure 7f; Grevemeyer et al., 2018). Instead, the Vp-depth distribution is more similar to that of Domain III crust near the ELSC (cf. red, dashed line in Figure 7f; Dunn & Martinez, 2011) around 20°S in the Lau Basin. It appears more reasonable that the composition of the upper crust inside the FRSC is intermediate between the endmembers of typical oceanic crust and andesitic back-arc crust. Thus, the upper crust is likely a mix of basalts, as dredged in the center of the FRSC by Keller et al. (2008), and volcanic arc rocks such as andesite.

The MCS data from the FRSC median valley show several sediment-filled ponds, bounded by normal faults and a number of features, which we interpret as extrusive mounds (Figure 8). The strata in two of the sediment-filled ponds are tilted (between 166 and 169 km and between 170 and 172 km along the profile; Figure 8), which is an indication of recent tectonic activity. A zone of high reflectivity is present near the center of the FRSC axial valley, between 173 and 175 km distance along our profile (Figure 8) that is likely associated with some features that we interpret as relatively recent lava flows on the seafloor.

The magnetic data along the profile BGR18-2R3 reveal a single positive anomaly, centered over the FRSC axial valley (Figure 7e). It is important to notice that no further geomagnetic reversals are recorded inside the FRSC. Following the plate kinematic model of Sleeper and Martinez (2016), the current opening rate of the FRSC ranges around 10 mm $year^{-1}$ at 17°20′S, where our profile crosses. This opening rate together with the ~30 km spanning width of the FRSC suggests that extension started roughly 1.5 Ma ago. The last

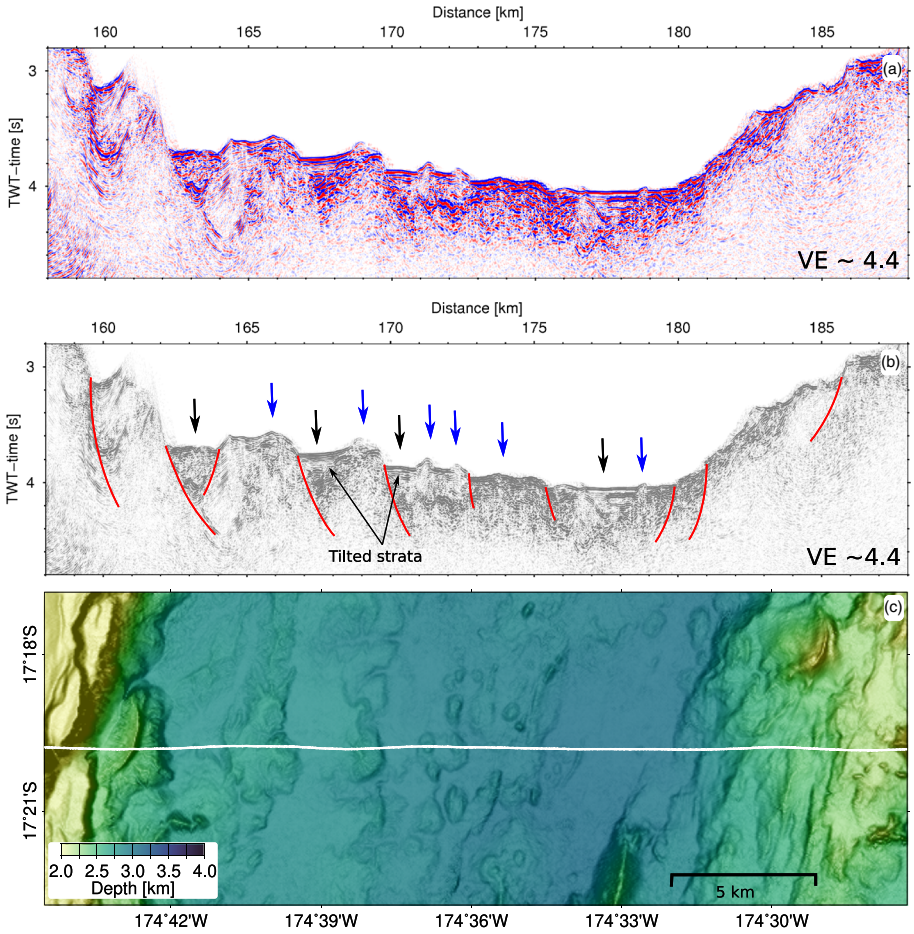

Figure 8. (a) Migrated MCS data section covering the FRSC axial valley. (b) Interpreted section with normal faults indicated by solid red lines. Black arrows indicate locations of sediment ponds. Blue arrows indicate locations of magmatic extrusions, interpreted from the hydroacoustic facies. (c) Bathymetry of the region covered by the two panels above. Solid white line represents the profile location. The location of the displayed profile section is also indicated on Figure 7b.

geomagnetic reversal, marking the transition from the Matuyama to the Bruhnes chron dates to 0.78 Ma (Bassinot et al., 1994) but is apparently not recorded in the FRSC crust. The absence of this reversal in the FRSC crust implies that the FRSC may have opened at much faster rates than predicted by the kinematic model of Sleeper and Martinez (2016). Another explanation is that crustal accretion inside the FRSC has until recently not enabled the recording of the magnetic field and was is different from magmatic crustal accretion at midoceanic spreading centers.

We now elaborate on possible scenarios of past crustal accretion at the southern portion of the FRSC. Sleeper et al. (2016) proposed that magmatism and along-axis segmentation at the southern FRSC may work similar to ultraslow spreading mid-ocean ridges (c.f., Cannat et al., 2008). Ultraslow spreading ridges have opening rates <~20 mm year^{-1}, which is the most obvious similarity to the southern FRSC. Another similarity of both systems is the along axis magmatic segmentation, illustrated by the occurrence of elevated volcanic centers and intermediate regions where the valley floor is deepened (Figure 7a). However, the locations of volcanic centers at the southern FRSC correlate with the locations of arc volcanoes (Figure 7a). According to Keller et al. (2008) the arc volcanoes K, J North, J South, and I (Figures 1 and 7a) are currently inactive since their tops are covered by carbonates, and there is no morphologic evidence for recent volcanic activity. Keller et al. (2008) further suspect that the proximal volcanic centers at the FRSC may at present be capturing the arc melts from these volcanoes. In reference to these findings, we propose that the magmatic segmentation at the southern FRSC is mostly influenced by the melt supply from the near Tofua Volcanic Arc, as was previously discussed by Sleeper et al. (2016).

At tectonically dominated segments of ultraslow spreading ridges, which would be an analogue to the FRSC region crossed by profile BGR18-2R3, the igneous crust is usually thinner than 6.5 km (Jokat & Schmidt-Aursch, 2007) and a clear Moho reflector is absent (Harding et al., 2017). However, we observe a strong Moho reflector inside the southern FRSC, and the crust is not significantly thinner than typical oceanic crust of 6.5–7.5 km thickness (Christeson et al., 2019; Grevemeyer et al., 2018; White et al., 1992). *P* wave velocities in the FRSC lower crust range between 7.2 and 7.4 km s^{-1} (Figure 7f), which is slightly elevated in comparison to typical oceanic crust (Christeson et al., 2019; Grevemeyer et al., 2018; White et al., 1992) but similar to lower crustal velocities identified in Domain II crust at the ELSC (Arai & Dunn, 2014). Mantle melting models suggest that high-velocity lower crust in Domain II near the ELSC is associated with elevated water content in the melting region, which leads to crystallization of unusual mafic cumulates in the lower crust (Eason & Dunn, 2015). Basalts from the FRSC carry an arc-like geochemical signature (Keller et al., 2008), and the volcanic front is at a relatively close distance to the center of the FRSC (~61 km). We propose that slab-derived water in the parental mantle melts may have caused the crystallization of high-velocity, mafic cumulates in the lower crust of the FRSC, similar to the processes postulated for the creation of Domain II lower crust at the ELSC (Eason & Dunn, 2015).

Based on our findings of the crustal structure at the southern end of the FRSC and the above considerations, we infer that past crustal accretion processes in this region had less in common with (ultraslow) midocean spreading centers than previously suggested by Sleeper et al. (2016). Instead, crustal accretion at the southern end of the FRSC was likely governed by a combination of extension of volcanic arc crust, mafic intrusive magmatism in the lower crust and unfocused extrusive activity.

We propose the following scenario for the evolution of the southern FRSC. In the wake of the initial rifting of arc crust, the east-west extension was accommodated by a combination of crustal thinning and magmatic accretion, the contributions of which vary between individual segments along the southern FRSC. The ~9.5 km thick crust and the andesitic composition of the high-standing rift shoulders indicate that they are part of the volcanic arc crust and were formed by slab-derived melts. In response to the initial rifting of the volcanic arc ~1.5 Ma ago, slab-derived melts were likely partitioned into one fraction feeding the Tofua Volcanic arc and another fraction migrating laterally towards the newly opened FRSC (Keller et al., 2008). The transition towards an increasingly basaltic composition of the upper crust inside the FRSC (Keller et al., 2008) could reflect an increase in the lithospheric extension, which in turn initiates decompression melting and mantle upwelling beneath the FRSC (Sleeper et al., 2016).

5.2. Crustal Structure of the Back-Arc Region (Southern Niuafo'ou Microplate)

To visualize lateral changes in the Vp-depth distribution of the back-arc crust, we establish an average Vp-depth profile for the igneous basement (Vp > 2.5 km s^{-1}) in the region between 5 and 160 km distance along our profile, which is plotted as black solid line in Figure 9e. We then subtracted this average Vp-depth profile from the final tomography model, and the resulting plot of Vp-deviations illuminates lateral variations in the Vp-depth structure of the back-arc crust (Figure 9c). The strongest deviations in the Vp-depth structure are present in the upper crust. These deviations do partly correlate with the seafloor topography and fabric along the profile. We identify four different tectonic zones in the back-arc along our profile, indicated by gray bars on top of Figures 9b and 9c.

We now describe and discuss these zones starting with the easternmost one. This region immediately west of the FRSC, between 140 and 155 km distance along our profile, shows reduced Vp-values throughout the crust and comprises the western rift shoulder of the FRSC. As discussed in section 5.1, we anticipate that the crust is mainly composed of andesitic lithologies and consider this block is a fragment of arc crust, rifted away from the Tofua Volcanic Arc by the FRSC (Figure 9c).

The zone between 118 and 140 km distance along our profile is characterized by a 7.9 ± 0.4 km thick crust with increased *P* wave velocities in the upper crust that are similar to the Vp-depth distribution of typical oceanic crust (solid blue line in Figure 9e). The basement surface in this zone is mostly smooth and overlain by well-stratified sediments, which create a very even seafloor that includes numerous small mounds (Figures 9aa and 10). Such a mound is present near 120 km along our profile, and its internal structure, imaged by MCS and subbottom profiler data, shows two bright spots with polarity identical to the seafloor reflector (Figure 10). We interpret these bright-spots as magmatic intrusions of

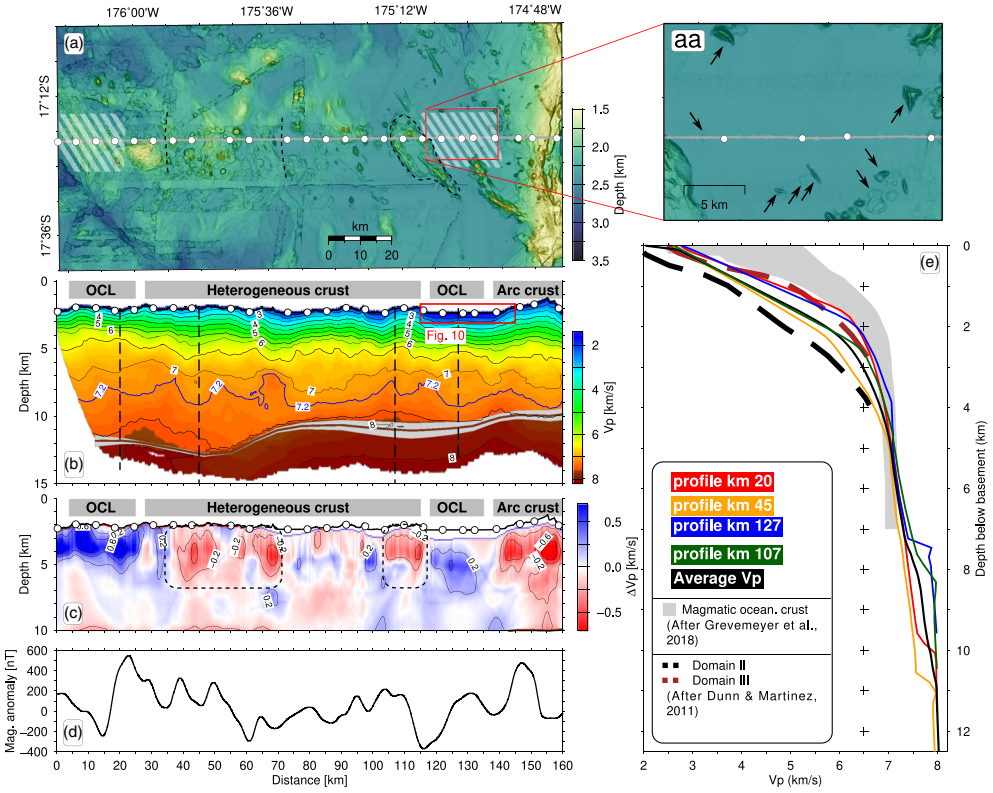

Figure 9. (a) Bathymetry of the back-arc region covered by profile BGR18-2R3 (gray line, white circles show OBS locations). Hatched areas indicate regions where the upper crust has a Vp-depth distribution similar to typical oceanic crust. Stippled polygon and lines correspond to polygons in panel c and indicate areas of decreased Vp in the upper crust. It should be noted, that findings from the profile are extrapolated off-profile in the hatched and stippled areas. (aa) Zoom-in to the back-arc area covered by sediments. Black arrows indicate locations of small mounds and ridges peeking through the sediment cover which are interpreted to be of volcanic origin. (b) *P* wave velocity model for the back-arc region with identified subdomains indicated by gray bars on top. OCL = oceanic crust like. Vertical dashed lines represent locations of 1-D Vp profiles plotted in panel e. (c) Velocity deviation in the igneous basement in reference to an average 1-D Vp-depth profile (solid black line in panel e). Contours are spaced at 0.2 km s^{-1}. Absolute values of calculated Vp deviations deeper than 10 km below sea surface are not plotted, since the variation in crustal thickness along the profile impose a bias at these depths. (d) Magnetic anomalies along profile BGR18-2R3 based on towed magnetometer data from the SO267 expedition. (e) 1-D Vp-depth profiles for different locations on the back-arc, indicated by dashed lines in panel b. Other 1-D velocity profiles are taken from the publications stated at the lower left of the plot. Note that all 1-D velocity profiles are taken from below basement surface.

horizontally extended geometry, which are commonly referred to as magmatic sills. Sediment strata above the magmatic sill are disturbed and bend slightly upwards where they are in contact with what we interpret as an intrusive body (Figure 10). We suggest that the intrusion has likely penetrated into sediments and is of younger relative-age than the surrounding sedimentary deposits. The seafloor morphology off-profile BGR18-2R3 shows several small mounds and ridges in the surrounding sediment-filled basin (highlighted in Figure 9aa) suggesting that postsedimentary intrusions are typical in this area (Figure 9aa). In the sediment-filled basin shown in Figure 10, the MCS section and subbottom profiler data show several buried normal faults indicating that crustal extension was still ongoing while sediments were deposited. The fault near 124 km along our profile extends down into the basement and supports the above statement. The fact that normal faults do not reach the seafloor indicates that the most-recent phase was characterized by tectonic quiescence. The area of smooth seafloor, revealed by bathymetry data, suggests that crust of similar fabric and origin covers a significant portion of the southeastern part of the Niuafo'ou Microplate. We highlight this zone to approximately 10 km north and south of our profile by a hatched polygon on Figure 9a. We postulate that seafloor spreading processes created the crust in this zone, which is supported by the Vp-depth profile and the smooth basement surface. However, the location of the spreading center creating this zone remains unclear, and the inferred magmatic intrusion (Figure 10) as well as the buried faults

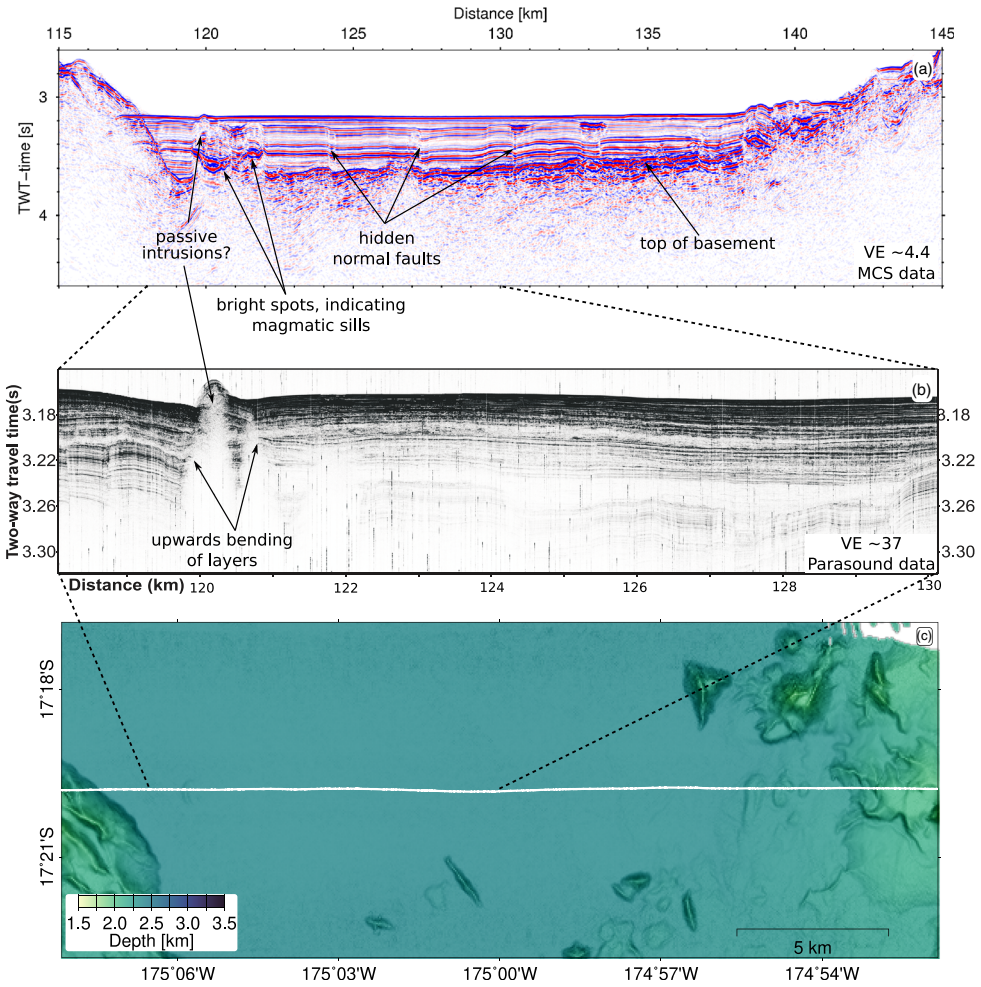

Figure 10. (a) Close-up view of the time-migrated MCS profile section crossing a sediment-filled basin on the back-arc with a feature that we interpret as a magmatic intrusion. The location along profile BGR18-2R3 is indicated in Figure 9b. (b) Record section of the Parasound parametric sediment-echosounder, covering a part of the MCS section above. Note the upwards bending of the sediment layers where they are in contact with the intrusive body, indicated by the arrows. (c) Bathymetry of the region covered by panel a. Solid white line represents the profile location.

indicates that magmatism and tectonism have remained active in this zone after crustal accretion had finalized.

The zone between 25 and 118 km along our profile is characterized by a heterogeneous upper crust in which two areas, between 32–70 and 100–115 km along our profile, indicated by stippled lines and polygons Figures 9a and 9c, stick out and show reduced *P* wave velocities throughout the upper crust. The Vp-depth distribution in these two crustal blocks is more similar with Domain II crust near the ELSC (compare solid orange line and stippled black line in Figure 9e; Dunn & Martinez, 2011) that with typical oceanic crust. The accretion of Domain II crust near the ELSC is strongly influenced by slab-derived water leaking into the melting zone of the back-arc spreading center (Eason & Dunn, 2015). This elevated water content enhances mantle melting, which leads to a thickened crust and a thick layer of basaltic (or even andesitic) rocks with increased porosity in the upper crust (Eason & Dunn, 2015; Hirth & Kohlstedt, 1996). Dunn and Martinez (2011) and Eason and Dunn (2015) introduced the term volcanic layer when referring to this specific layer of the upper crust identified near the ELSC. Considering the similarity to Domain II crust, we propose that these two crustal blocks between 32–70 and 100–115 km distance along our profile might have been produced at a spreading center, likely in proximity to the active arc volcanic front, which was influenced by slab-derived water. Alternatively, these two crustal blocks could also represent

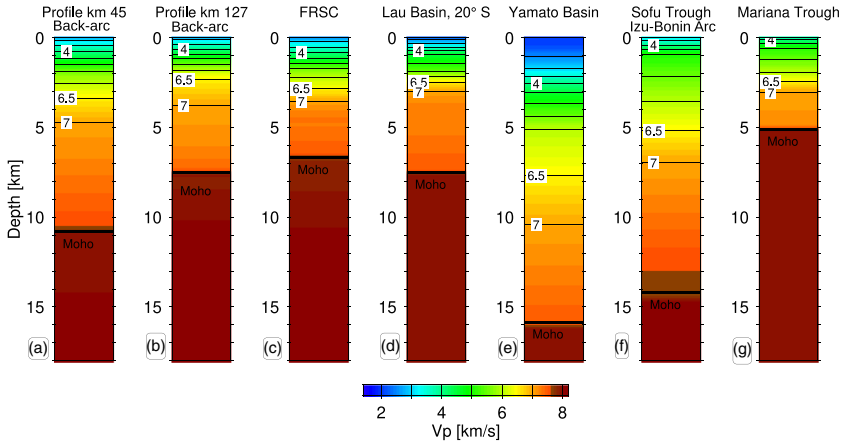

Figure 11. Comparison of 1-D velocity profiles from the back-arc and FRSC with profiles from other back-arc regions. Profiles (a–c) from this study and represent averages over a range of 7 km along the profile at indicated locations. (d) Represents average back-arc crust near the Eastern Lau Spreading Center between 20° and 21° from Arai and Dunn (2014). (e) Represents crust from the Yamato Basin where continental crust is rifted T Sato et al. (2014). (f) Represents crust in the Sofu Trough behind the Izu-Bonin Arc, from Takahashi et al. (2011). (g) Represents crust in the Mariana Trough behind the Mariana Arc, from Takahashi et al. (2008).

fragments of arc crust, which have been rifted away from the active arc just like the crustal fragment between 140 and 155 km along our profile that constitutes the western rift shoulder of the FRSC (Figure 9). Both scenarios have in common that the two crustal blocks have been created at or near the active volcanic arc.

The zone between 0 and 23 km along our profile shows elevated *P* wave velocities in the upper crust that are similar to typical oceanic crust (labeled as oceanic crust like (OCL) in Figure 9e; Grevemeyer et al., 2018). Approximately 50 km west of profile BGR18-2R3 is the oblique opening LETZ (Figure 1). We suggest that the zone between 0 and 23 km along our profile has been created through seafloor spreading processes at the LETZ or another preceding spreading center west of our survey area.

5.3. Magmatic Underplating in the Back-Arc Region

Our *P* wave tomography model indicates that high-velocity (Vp 7.2–7.5 km s^{-1}) lower crustal units are present in some places of the back-arc region (Figure 9e). Such lower crustal high-velocity layers are typically observed at volcanic continental margins, for example in the North Atlantic where the high-velocity lower crust may be up to 25 km thick (Breivik et al., 2014; Kelemen & Holbrook, 1995; Mjelde et al., 2002). High-velocity lower crustal units have also been identified in other back-arc regions including the Izu-Bonin back-arc (Figure 11; Takahashi et al., 2008), the Yamato Basin in the Japan Sea (Figure 11e; T Sato et al., 2014) and some locations of the Lau Basin crust at 20°30′S (Figure 11d; Arai & Dunn, 2014). The anomalously high *P* wave velocities in the lower crust are indicative of magmatic underplating, a process during which melts are trapped at the base of the lower crust where they crystallize as mafic cumulates. Anomalies of increased mantle potential temperatures and/or increased crystalline water in the upper mantle promote the creation of partial melts at mantle depths, which may then ascend into the lower crust and lead to magmatic underplating (Eason & Dunn, 2015; T Sato et al., 2014; Takahashi et al., 2008). Passive seismological studies revealed decreased *P* and *S* wave velocities (Wei et al., 2015; Wiens et al., 2008) and elevated attenuation (Bowman, 1988; Roth et al., 1999; Wei & Wiens, 2018) in the upper mantle below the northeastern Lau Basin. These anomalies are reported in reference to typical oceanic upper mantle (Wei et al., 2015). In particular, decreased *S* wave velocities and elevated seismic attenuation in the upper mantle are both interpreted as indicators for elevated potential temperatures (H Sato et al., 2012). Thus, increased concentrations of partial melt in the upper mantle beneath the northeastern Lau Basin (Wei et al., 2015) support the magmatic underplating we observe along our profile (Figure 9e).

6. Conclusions

This study presents seismic and gravimetric results of a 290 km long east-west oriented geophysical transect through the northeastern Lau Basin at 17°20′S that crosses the southern portion of the Niuafo'ou Microplate, the southern end of the FRSC, and the Tofua Volcanic Arc. We focus on the crustal structure in this region about which very little was previously known. Our main results include the following:

1. Lateral variations in the Vp-depth distribution across the FRSC and the adjacent rift shoulders suggest that the crust inside the rift is of intermediate composition between andesitic arc crust and typical basaltic oceanic crust. Reduced crustal densities inside the FRSC may best be explained by a thermal anomaly. We conclude that the crust inside the southern FRSC was created through a combination of extension of arc crust and intrusive magmatism, the contributions of which vary between different segments along the FRSC. Past crustal accretion inside the southern FRSC had therefore less in common with (ultraslow) midoceanic spreading centers than previously suggested. A continuous Moho reflector was observed beneath the FRSC, an observation that is not common for spreading centers and supports our interpretation.
2. A detailed analysis of the Vp-depth distributions across the southern portion of the Niuafo'ou Microplate revealed a heterogeneous back-arc crust composed of several distinct crustal blocks. The crust immediately west of the FRSC rift shoulders shows a smooth basement surface and has a Vp-depth distribution similar to typical oceanic crust leading us to the conclusion that this region has been created by typical seafloor spreading. Scattered magmatic intrusions and hidden normal faults in the sediments covering the basement in this zone indicate that tectonic extension and magmatism have been active here until recently. Further west is a zone that includes crustal blocks of a Vp-depth distribution similar to arc crust or crust created in proximity to the arc, where the spreading center was influenced by slab-derived water. We conclude that these portions of back-arc crust were either rifted away from the active arc or represent a 'hydrous' type of oceanic crust, which has previously been identified at the ELSC, near 20°S (Arai & Dunn, 2014). Towards the LETZ, the Vp-depth distribution is again more similar to typical oceanic crust which leads us to conclude that back-arc crust in this region has been created through seafloor spreading at the LETZ or at a preceding spreading center in this region.
3. We interpret the existence of high-velocity lower crustal units in some parts of the investigated portion of the southern Niuafo'ou Microplate as evidence for magmatic underplating in this region. The processes of magmatic underplating are promoted by a previously identified anomaly in mantle potential temperatures underneath this region.

Acknowledgments

We are grateful to the captain and crew of RV Sonne for their support during expedition SO267. Special thanks are dedicated to all the scientists (including M. Engelbert-Stewart, F. Hampel, R. Hartmann, A. Jegen, P. Mercier-Langevin, B. Schramm, F. Petersen, S. Petersen, C. Rahmsdorf, M. Weber) helping with the logistics and operation of the OBSs. We are indebted to the Tongan observer, T. Fangatua. Insightful comments and suggestions by B. Shuck, one anonymous reviewer and the associate editor greatly improved this manuscript. This study and expedition SO267 was financially supported by the German Ministry of Science and Education (Bundesministerium für Bildung und Forschung (BMBF), grants 03G0267A and 03G0267B) and additional support from GEOMAR Helmholtz Centre for Ocean Research Kiel and the Federal Institute for Geosciences and Natural Resources, Hannover (BGR). Figures have been created with the GMT software (Wessel et al., 2013).

Data Availability Statement

OBS, bathymetry, and Parasound data will be available from PANGAEA (https://www.pangaea.de) after an embargo period ending in 2021. MCS and gravity data will be available from the GEO-SEAS database (https://www.geo-seas.eu) after an embargo period ending in 2021.

References

Arai, R., & Dunn, R. A. (2014). Seismological study of Lau back arc crust: Mantle water, magmatic differentiation, and a compositionally zoned basin. *Earth and Planetary Science Letters*, *390*, 304–317. https://doi.org/10.1016/j.epsl.2014.01.014

Baker, E. T., Walker, S. L., Massoth, G. J., & Resing, J. A. (2019). The NE Lau Basin: Widespread and abundant hydrothermal venting in the Back-arc region behind a superfast Subduction zone. *Frontiers in Marine Science*, *6*(July), 1–15. https://doi.org/10.3389/fmars.2019.00382

Bassett, D., Kopp, H., Sutherland, R., Henrys, S., Watts, A. B., Timm, C., et al. (2016). Crustal structure of the Kermadec arc from MANGO seismic refraction profiles. *Journal of Geophysical Research: Solid Earth*, *121*, 7514–7546. https://doi.org/10.1002/2016JB013194

Bassett, D., & Watts, A. B. (2015). Gravity anomalies, crustal structure, and seismicity at subduction zones: 1. Seafloor roughness and subducting relief. *Geochemistry, Geophysics, Geosystems*, *16*, 1508–1540. https://doi.org/10.1002/2014GC005684

Bassinot, F. C., Labeyrie, L. D., Vincent, E., Quidelleur, X., Shackleton, N. J., & Lancelot, Y. (1994). The astronomical theory of climate and the age of the Brunhes-Matuyama magnetic reversal. *Earth and Planetary Science Letters*, *126*(1–3), 91–108. https://doi.org/10.1016/0012-821X(94)90244-5

Baxter, A. T., Hannington, M. D., Stewart, M. S., Emberley, J. M., Breker, K., Krätschell, A., et al. (2020). Shallow seismicity and the classification of structures in the Lau back-arc basin. *Geochemistry, Geophysics, Geosystems*,21, e2020GC008924. https://doi.org/10.1029/2020gc008924

Bevis, M., Taylor, F. W., Schutz, B. E., Recy, J., Isacks, B. L., Helu, S., et al. (1995). Geodetic observations of very rapid convergence and back-arc extension at the Tonga arc. *Nature*, *374*(6519), 249–251. https://doi.org/10.1038/374249a0

Bowman, J. R. (1988). Body wave attenuation in the Tonga subduction zone. *Journal of Geophysical Research*, *93*(B3), 2125–2139. https://doi.org/10.1029/JB093iB03p02125

Brandl, P. A., Schmid, F., Augustin, N., Grevemeyer, I., Arculus, R. J., Devey, C. W., et al. (2020). The 6–8 Aug 2019 eruption of 'volcano F' in the Tofua arc, Tonga. *Journal of Volcanology and Geothermal Research*, *390*, 106695. https://doi.org/10.1016/j.jvolgeores.2019.106695

Breivik, A., Faleide, J. I., Mjelde, R., Flueh, E., & Murai, Y. (2014). Magmatic development of the outer Vøring margin from seismic data. *Journal of Geophysical Research: Solid Earth*, *119*, 6733–6755. https://doi.org/10.1002/2014JB011040

Brocher, T. M. (2005). Empirical relations between elastic wavespeeds and density in the Earth's crust. *Bulletin of the Seismological Society of America*, *95*(6), 2081–2092. https://doi.org/10.1785/0120050077

Cannat, M., Sauter, D., Bezos, A., Meyzen, C., Humler, E., & le Rigoleur, M. (2008). Spreading rate, spreading obliquity, and melt supply at the ultraslow spreading southwest Indian ridge. *Geochemistry, Geophysics, Geosystems*, *9*, Q04002. https://doi.org/10.1029/2007gc001676

Carlson, R. L. (2004). Influence of pressure and mineralogy on seismic velocities in oceanic gabbros: Implications for the composition and state of the lower oceanic crust. *Journal of Geophysical Research*, *109*, B0925. https://doi.org/10.1029/2003jb002699

Carlson, R. L., & Raskin, G. S. (1984). Density of the ocean crust. *Nature*, *311*(5986), 555–558. https://doi.org/10.1038/311555a0

Chadwick, W. W., Rubin, K. H., Merle, S. G., Bobbitt, A. M., Kwasnitschka, T., & Embley, R. W. (2019). Recent eruptions between 2012 and 2018 discovered at west mata submarine volcano (NE Lau Basin, SW Pacific) and characterized by new ship, AUV, and ROV data. *Frontiers in Marine Science*, *6*(495). https://doi.org/10.3389/fmars.2019.00495

Chase, C. G. (1971). Tectonic history of the Fiji plateau. *Bulletin of the Geological Society of America*, *82*(11), 3087–3110. https://doi.org/10.1130/0016-7606(1971)82

Christensen, N. I. (1996). Poisson's ratio and crustal seismology. *Journal of Geophysical Research*, *101*(B2), 3139–3156. https://doi.org/10.1029/95jb03446

Christeson, G. L., Goff, J. A., & Reece, R. S. (2019). Synthesis of oceanic crustal structure from two-dimensional seismic profiles. *Reviews of Geophysics*, *57*, 504–529. https://doi.org/10.1029/2019RG000641

Conder, J. A., & Wiens, D. A. (2011). Shallow seismicity and tectonics of the central and northern Lau Basin. *Earth and Planetary Science Letters*, *304*(3–4), 538–546. https://doi.org/10.1016/j.epsl.2011.02.032

Crawford, W. C., Hildebrand, J. A., Dorman, L. M., Webb, S. C., & Wiens, D. A. (2003). Tonga ridge and Lau Basin crustal structure from seismic refraction data. *Journal of Geophysical Research*, *108*(B4), 2195. https://doi.org/10.1029/2001jb001435

Dunn, R. A., & Martinez, F. (2011). Contrasting crustal production and rapid mantle transitions beneath back-arc ridges. *Nature*, *469*(7329), 198–202. https://doi.org/10.1038/nature09690

Dunn, R. A., Martinez, F., & Conder, J. A. (2013). Crustal construction and magma chamber properties along the Eastern Lau Spreading Center. *Earth and Planetary Science Letters*, *371-372*, 112–124. https://doi.org/10.1016/j.epsl.2013.04.008

Eason, D. E., & Dunn, R. A. (2015). Petrogenesis and structure of oceanic crust in the Lau back-arc basin. *Earth and Planetary Science Letters*, *429*, 128–138. https://doi.org/10.1016/j.epsl.2015.07.065

Escrig, S., Bézos, A., Langmuir, C. H., Michael, P. J., & Arculus, R. (2012). Characterizing the effect of mantle source, subduction input and melting in the Fonualei Spreading Center, Lau Basin: Constraints on the origin of the boninitic signature of the back-arc lavas. *Geochemistry, Geophysics, Geosystems*, *13*, Q10008. https://doi.org/10.1029/2012GC004130

German, C. R., Baker, E. T., Connelly, D. P., Lupton, J. E., Resing, J., Prien, R. D., et al. (2006). Hydrothermal exploration of the Fonualei Rift and Spreading Center and the Northeast Lau Spreading Center. *Geochemistry, Geophysics, Geosystems*, *7*, Q11022. https://doi.org/10.1029/2006GC001324

Grevemeyer, I., Ranero, C. R., & Ivandic, M. (2018). Structure of oceanic crust and serpentinization at subduction trenches. *Geosphere*, *14*(2), 395–418. https://doi.org/10.1130/GES01537.1

Hannington, M. D., H. Kopp, and M. Schnabel (2019), RV SONNE Cruise Report SO267: ARCHIMEDES I: Arc Rifting, Metallogeny and Microplate Evolution – an Integrated Geodynamic, Magmatic and Hydrothermal Study of the Fonualei Rift System, NE Lau Basin, Suva (Fiji) – Suva (Fiji), 11.12.2018–26.01.2019*Rep*., Kiel.

Harding, J. L., Van Avendonk, H. J. A., Hayman, N. W., Grevemeyer, I., Peirce, C., & Dannowski, A. (2017). Magmatic-tectonic conditions for hydrothermal venting on an ultraslow-spread oceanic core complex. *Geology*, *45*(9), 839–842. https://doi.org/10.1130/g39045.1

Hawkins, J. W. (1995). Evolution of the Lau Basin-insights from ODP leg 135. *Geophysical Monograph Series*, *88*, 125–173. https://doi.org/10.1029/GM088p0125

Hirth, G., & Kohlstedt, D. L. (1996). Water in the oceanic mantle: Implications for rheology, melt extraction and the evolution of the lithosphere. *Earth and Planetary Science Letters*, *144*(1-2), 93–108. https://doi.org/10.1016/0012-821X(96)00154-9

Jokat, W., & Schmidt-Aursch, M. C. (2007). Geophysical characteristics of the ultraslow spreading Gakkel ridge, Arctic Ocean. *Geophysical Journal International*, *168*(3), 983–998. https://doi.org/10.1111/j.1365-246X.2006.03278.x

Karig, D. E. (1970). Ridges and basins of the Tonga-Kermadec Island Arc System. *Journal of Geophysical Research (1896–1977)*, *75*(2), 239–254. https://doi.org/10.1029/JB075i002p00239

Kelemen, P. B., & Holbrook, W. S. (1995). Origin of thick, high-velocity igneous crust along the U.S. East Coast Margin. *Journal of Geophysical Research*, *100*(B6), 10077–10094. https://doi.org/10.1029/95JB00924

Keller, N. S., Arculus, R. J., Hermann, J., & Richards, S. (2008). Submarine back-arc lava with arc signature: Fonualei spreading Center, northeast Lau Basin, Tonga. *Journal of Geophysical Research*, *113*, B08S07. https://doi.org/10.1029/2007JB005451

Kern, H. M. (1993). Physical properties of crustal and upper mantle rocks with regards to lithosphere dynamics and high pressure mineralogy. *Physics of the Earth and Planetary Interiors*, *79*(1–2), 113–136. https://doi.org/10.1016/0031-9201(93)90145-Y

Kim, J., Son, S. K., Son, J. W., Kim, K. H., Shim, W. J., Kim, C. H., & Lee, K. Y. (2009). Venting sites along the Fonualei and Northeast Lau Spreading Centers and evidence of hydrothermal activity at an off-axis caldera in the northeastern Lau Basin. *Geochemical Journal*, *43*(1), 1–13. https://doi.org/10.2343/geochemj.0.0164

Korenaga, J., Holbrook, W. S., Detrick, R. S., & Kelemen, P. B. (2001). Gravity anomalies and crustal structure at the southeast Greenland margin. *Journal of Geophysical Research*, *106*(B5), 8853–8870. https://doi.org/10.1029/2000jb900416

Korenaga, J., Holbrook, W. S., Kent, G. M., Kelemen, P. B., Detrick, R. S., Larsen, H. C., et al. (2000). Crustal structure of the southeast Greenland margin from joint refraction and reflection seismic tomography. *Journal of Geophysical Research*, *105*(B9), 21591–21614. https://doi.org/10.1029/2000jb900188

Ludwig, W. J., Nafe, J. E., & Drake, C. L. (1970). Seismic refraction. In *The Sea*, Edited, (pp. 53–84). New York: Wiley-interscience.

Mjelde, R., Kasahara, J., Shimamura, H., Kamimura, A., Kanazawa, T., Kodaira, S., et al. (2002). Lower crustal seismic velocity-anomalies; magmatic underplating or serpentinized peridotite? Evidence from the Vøring Margin, NE Atlantic. *Marine Geophysical Researches*, *23*(2), 169–183. https://doi.org/10.1023/A:1022480304527

Roth, E. G., Wiens, D. A., Dorman, L. M., & Webb, C. (1999). Seismic attenuation in the Tonga-Fiji region using phase pair methods. *Journal of Geophysical Research*, *104*(B3), 4795–4809. https://doi.org/10.1029/1998jb900052

Ryan, W. B. F., Carbotte, S. M., Coplan, J. O., O'Hara, S., Melkonian, A., Arko, R., et al. (2009). Global multi-resolution topography synthesis. *Geochemistry, Geophysics, Geosystems*, *10*, Q03014. https://doi.org/10.1029/2008GC002332

Sandwell, D. T., Müller, R. D., Smith, W. H. F., Garcia, E., & Francis, R. (2014). New global marine gravity model from CryoSat-2 and Jason-1 reveals buried tectonic structure. *Science*, *346*(6205), 65–67. https://doi.org/10.1126/science.1258213

Sato, H., M. Fehler, and T. Maeda (2012), Seismic wave propagation and scattering in the heterogeneous earth, 1–494 pp.

Sato, T., No, T., Kodeira, S., Takahashi, N., & Kaneda, Y. (2014). Seismic constraints of the formation processon the back-arc basin in the southeastern Japan Sea. *Journal of Geophysical Research: Solid Earth*, *119*, 1563–1579. https://doi.org/10.1002/2013JB010643

Sleep, N. H., & Warren, J. M. (2014). Effect of latent heat of freezing on crustal generation at low spreading rates. *Geochemistry, Geophysics, Geosystems*, *15*, 3161–3174. https://doi.org/10.1002/2014GC005423

Sleeper, J. D., & Martinez, F. (2016). Geology and kinematics of the Niuafo'ou microplate in the northern Lau Basin. *Journal of Geophysical Research: Solid Earth*, *121*, 4852–4875. https://doi.org/10.1002/2016JB013051

Sleeper, J. D., Martinez, F., & Arculus, R. (2016). The Fonualei rift and spreading Center: Effects of ultraslow spreading and arc proximity on back-arc crustal accretion. *Journal of Geophysical Research: Solid Earth*, *121*, 4814–4835. https://doi.org/10.1002/2016JB013050

Takahashi, N., Kodaira, S., Tatsumi, Y., Kaneda, Y., & Suyehiro, K. (2008). Structure and growth of the Izu-Bonin-Mariana arc crust: 1. Seismic constraint on crust and mantle structure of the Mariana arc-back-arc system. *Journal of Geophysical Research*, *113*, B01104. https://doi.org/10.1029/2007JB005120

Takahashi, N., Yamashita, M., Kodaira, S., Miura, S., Sato, T., No, T., et al. (2011). Rifting structure of Central Izu-Ogasawara (Bonin) arc crust: Results of seismic crustal imaging. In Y. Ogawa, R. Anma, & Y. Dilek (Eds.), *Accretionary Prisms and Convergent Margin Tectonics in the Northwest Pacific Basin*, (pp. 75–95). Dordrecht: Springer Netherlands. https://doi.org/10.1007/978-90-481-8885-7_4

Taylor, B., Zellmer, K., Martinez, F., & Goodliffe, A. (1996). Sea-floor spreading in the Lau back-arc basin. *Earth and Planetary Science Letters*, *144*(1–2), 35–40. https://doi.org/10.1016/0012-821x(96)00148-3

Tontini, F. C., Bassett, D., Ronde, C. E. J. D., Timm, C., & Wysoczanski, R. (2019). Early evolution of a young back-arc basin in the Havre trough. *Nature Geoscience*, *12*(10), 856–862. https://doi.org/10.1038/s41561-019-0439-y

Wei, S. S., & Wiens, D. A. (2018). P-wave attenuation structure of the Lau back-arc basin and implications for mantle wedge processes. *Earth and Planetary Science Letters*, *502*, 187–199. https://doi.org/10.1016/j.epsl.2018.09.005

Wei, S. S., Wiens, D. A., Zha, Y., Plank, T., Webb, S. C., Blackman, D. K., et al. (2015). Seismic evidence of effects of water on melt transport in the Lau back-arc mantle. *Nature*, *518*(7539), 395–398. https://doi.org/10.1038/nature14113

Wessel, P., Smith, W. H. F., Scharroo, R., Luis, J., & Wobbe, F. (2013). Generic mapping tools: Improved version released. *Eos Transactions American Geophysical Union*, *94*(45), 409–410. https://doi.org/10.1002/2013EO450001

White, R. S., McKenzie, D., & O'Nions, R. K. (1992). Oceanic crustal thickness from seismic measurements and rare earth element inversions. *Journal of Geophysical Research*, *97*(B13), 19683. https://doi.org/10.1029/92jb01749

Wiens, D. A., Conder, J. A., & Faul, U. H. (2008). The seismic structure and dynamics of the mantle wedge. *Annual Review of Earth and Planetary Sciences*, *36*(1), 421–455. https://doi.org/10.1146/annurev.earth.33.092203.122633

Zellmer, K. E., & Taylor, B. (2001). A three-plate kinematic model for Lau Basin opening. *Geochemistry, Geophysics, Geosystems*, *2*(5). https://doi.org/10.1029/2000GC000106

Zelt, C. A., & Smith, R. B. (1992). Seismic traveltime inversion for 2-D crustal velocity structure. *Geophysical Journal International*, *108*(1), 16–34. https://doi.org/10.1111/j.1365-246X.1992.tb00836.x